



THE UNIVERSITY *of* EDINBURGH

Edinburgh Research Explorer

## Combining the Nonuniform Structure and Flow Maldistribution for the Accurate Prediction of the Process Performance of Monolithic Adsorbent Systems

**Citation for published version:**

Sharma, I, Mennitto, R, Friedrich, D & Brandani, S 2020, 'Combining the Nonuniform Structure and Flow Maldistribution for the Accurate Prediction of the Process Performance of Monolithic Adsorbent Systems', *Industrial & Engineering Chemistry Research*. <https://doi.org/10.1021/acs.iecr.9b05845>

**Digital Object Identifier (DOI):**

[10.1021/acs.iecr.9b05845](https://doi.org/10.1021/acs.iecr.9b05845)

**Link:**

[Link to publication record in Edinburgh Research Explorer](#)

**Document Version:**

Peer reviewed version

**Published In:**

Industrial & Engineering Chemistry Research

**General rights**

Copyright for the publications made accessible via the Edinburgh Research Explorer is retained by the author(s) and / or other copyright owners and it is a condition of accessing these publications that users recognise and abide by the legal requirements associated with these rights.

**Take down policy**

The University of Edinburgh has made every reasonable effort to ensure that Edinburgh Research Explorer content complies with UK legislation. If you believe that the public display of this file breaches copyright please contact [openaccess@ed.ac.uk](mailto:openaccess@ed.ac.uk) providing details, and we will remove access to the work immediately and investigate your claim.



# Combining the Nonuniform Structure and Flow Maldistribution for the Accurate Prediction of the Process Performance of Monolithic Adsorbent Systems

Ishan Sharma<sup>a</sup>, Daniel Friedrich<sup>a</sup> and Stefano Brandani<sup>a,\*</sup>

<sup>a</sup> School of Engineering, The University of Edinburgh, The King's Buildings, Edinburgh EH9 3FB, UK

## Abstract

Monolithic adsorbents are used to achieve the intensification of adsorption-based separation processes. The ideal monolith assumption, wherein the monolith is assumed to be composed of identical channels, is often made while modelling monolith adsorbent columns. However, the monolith production processes invariably introduce certain non-uniformities in channel size and adsorbent loadings. Such non-uniformities tend to broaden the breakthrough curve. The ideal monolith assumption, therefore, results in a sharper concentration front than what is experimentally observed. The mass transfer coefficient is often artificially reduced to match the broad experimental breakthrough curve. At the same time, to reasonably predict the full-cycle performance, the true mass transfer coefficient has to be used; this implies that different intrinsic parameters are needed to explain the same physical process. The present article aims to address this inherent inconsistency by taking into account the structural non-uniformities. A monolith consisting of corrugated channels has been used as a case study to illustrate this approach. All the monolith channels have been assumed to be grouped into different 'types', with each type corresponding to a particular channel size and adsorbent loading; this implies that the overall breakthrough curve has been assumed to be a combination of several breakthrough curves. By taking into account the structural non-uniformities and flow maldistribution, it has been shown that the true mass transfer coefficient can reasonably predict both the breakthrough and full-cycle performance. For the investigated case study, the full-cycle predictions via this approach were within  $\pm 2.5$  % of the experimental observations. Additionally, by accounting for the additional dispersion caused by channel non-uniformities, predictions are closer to the experimental observations at high throughput, as compared to the ideal monolith approach with true mass transfer coefficient. Since the primary application of monolith columns is in the intensification of adsorption processes, it becomes imperative to account for channel non-uniformities.

**Keywords:** Monolithic adsorbents; Breakthrough curve; Channel non-uniformities; Flow maldistribution; Fluid separation

\* Corresponding author at School of Engineering, The University of Edinburgh, The King's Buildings, Edinburgh EH9 3FB, UK. Email address: [s.brandani@ed.ac.uk](mailto:s.brandani@ed.ac.uk)

## Nomenclature and abbreviations

### *Symbols*

$A$ : Free cross-sectional area ( $\text{m}^2$ )

$a$ : Base length of the sinusoidal channel (m)

$b$ : Langmuir equilibrium constant (1/bar)

$c$ : Gas phase concentration ( $\text{mol}/\text{m}^3$ )

$D_{ch}$ : Characteristic dimension or the hydraulic diameter of the sinusoidal channel (m)

$D_m$ : Molecular diffusivity ( $\text{m}^2/\text{s}$ )

$f$ : Fanning friction factor

$F$ : Flow rate through different type of channels (mol/s)

$J$ : Diffusive flux ( $\text{mol}/\text{m}^2/\text{s}$ )

$k_{LDF}$ : LDF mass transfer coefficient (1/s)

$L$ : Length of the monolith column (m)

$N$ : Number of channels of a particular type

$NC$ : Number of components

$p$ : Partial pressure (bar)

$\bar{Q}$ : Average concentration in the adsorbent layer ( $\text{mol}/\text{m}^3$ )

$\bar{q}$ : Average adsorbed phase concentration ( $\text{mol}/\text{m}^3$ )

$q$ : Adsorbed phase concentration ( $\text{mol}/\text{m}^3$ )

$R$ : Universal gas constant ( $\text{J}/\text{mol}/\text{K}$ )

$Re$ : Reynolds number

$t$ : Time (s)

$T$ : Temperature (K)

$v$ : Interstitial velocity in the sinusoidal channel (m/s)

$y$ : Mole fraction

$y_0$ : Feed mole fraction

$z$ : Axial length (m)

### *Greek letters*

$\alpha$ : Aspect ratio of the sinusoidal channel

$\Delta\tilde{H}$ : Heat of adsorption ( $\text{J}/\text{mol}$ )

$\varepsilon$ : Porosity

$\eta$ : Dynamic viscosity of the gas (Pa s)

$\mu$ : First moment of the breakthrough curve (s)

#### *Subscript*

*avg*: Average value

*ad*: Adsorbent layer

*i*: Index for channel type,  $i = 1, 2 \dots n$

*bulk*: Bulk phase

*bypass*: Related to bypass stream

*j*: Index for component,  $j = 1, 2 \dots NC$

*f – bypass*: Feed flow, apart from the bypass flow

*T*: Total

*f*: Feed

#### *Superscript*

\*: Calculated at equilibrium

*exp*: Experimental

*l*: Index for the site in dual-site Langmuir isotherm

*sat*: At saturation

#### *Abbreviations*

RCPSA: Rapid Cycle Pressure Swing Adsorption

VPSA: Vacuum Pressure Swing Adsorption

MTC: Mass Transfer Coefficient

HR: Heavy Reflux

EqD: pressure equalisation depressurisation

CnD: counter-current depressurisation

LR: Light Reflux

EqU: pressure equalisation pressurisation

LPP: light product pressurisation

ECP: Experimental CO<sub>2</sub> Purity

SCP: Simulated CO<sub>2</sub> Purity

ECR: Experimental CO<sub>2</sub> Recovery

SCR: Simulated CO<sub>2</sub> Recovery

## Introduction

A significant reduction in cycle time is essential for the intensification of cyclic adsorption processes. One of the most effective means to achieve this is to increase the amount of feed processed per unit time. However, this results in a higher fluid superficial velocity and consequently, a higher pressure drop across adsorption beds filled with conventional adsorbent beads or pellets (Ruthven and Thaeon, 1997). A high-pressure drop is specifically detrimental for gas phase separations, as it means a significant loss of energy utilised in pressurisation. As a substitute to pelleted or beaded adsorbents in fast-cycle adsorption processes, structured adsorbents are used to reduce pressure drop gradient at high flow rates, while potentially reducing the mass transfer diffusion length as well. Additionally, structured adsorbents do not suffer from fluidisation at high superficial velocity, along with potentially high heat transfer rates (Ruthven and Thaeon, 1997). The adsorbents are typically structured in the form of monoliths, laminates, foams or fabrics (Rezaei and Webley, 2010).

Structured adsorbents have found extensive applications in catalysis. A classic example being a catalytic converter, typically used in vehicle exhaust systems. In contrast, commercial fluid separation applications have widely adopted structured adsorbents only recently. For example, Xebec Adsorption Inc., along with ExxonMobil Research and Engineering, has developed a Rapid Cycle Pressure Swing Adsorption (RCPSA) process for hydrogen recovery in refineries (Xebec, 2018). Xebec has also installed an off-shore natural gas conditioning unit employing structured adsorbents at Platform Gail, Santa Barbara Channel, USA (Toreja et al., 2010). More recently, Inventys Inc. has patented a process named VeloxoTherm<sup>TM</sup> (velox: fast; therm: thermal) for post-combustion CO<sub>2</sub> capture via a rapid TSA cycle (InvenTys Inc., 2017). The VeloxoTherm<sup>TM</sup> process is the first commercial post-combustion CO<sub>2</sub> capture process using structured adsorbent (Naturally Resourceful, 2017).

Structured adsorbents have enabled the application of adsorption technology where previously it was deemed infeasible due to high footprint and costs, necessitating the need to model the structured adsorbent-based separation processes accurately. Scientific studies often rely on certain simplifying assumptions to model such processes. For monolithic adsorbents, it is often assumed that all the channels have a uniform channel size and adsorbent loading (For example, Regufe et al., 2018 and Rezaei et al., 2010). Such a monolith, exhibiting uniformity of channel size and adsorbent loading has been referred to as an ‘ideal’ monolith in this article. An ideal monolith may be modelled as a single representative channel, thereby reducing the computation effort significantly (Lopes and Rodrigues, 2016). However, the assumption of an ideal monolith may be invalid if there exists a significant non-uniformity in channel size and adsorbent loading. Such non-uniformities are invariably introduced due to slight variances in the production process of a ‘real’ monolith (Gulijk et al., 2005). Hence, it is often imperative to account for such non-uniformities, the effect of which may be significant, as recently noted by Mohammadi (2017). A non-uniformity in channel size results in different interstitial flow velocities in channels with different size, while a non-uniform adsorbent loading also means that the fluid has a non-uniform mean residence time across different channels. As a result, the monolith breakthrough can be viewed as a combination of several distinct breakthrough curves. The net effect of channel non-uniformities is an additional dispersion observed in the monolith’s breakthrough curve, which the uniform channel model cannot explain.

An 'effective' diffusivity is often used to match the experimental breakthrough curve with the uniform channel model. A recent example of this being the corrugated monolith studied by Mohammadi (2017) in which they artificially lowered the true Mass Transfer Coefficient (MTC), measured independently using frequency response experiments. They also noted that the lower MTC, though able to predict the breakthrough, grossly under-estimated the Vacuum Pressure Swing Adsorption (VPSA) cycle's performance. They were able to reasonably predict the cycle performance only with the true MTC, rather than the reduced one. Additionally, even with the real MTC, they observed significant disagreement between their model predictions and experimental observations at high throughput. They attributed this disagreement to the non-uniformity of channels in the monolith but did not provide a quantitative explanation for the same.

There is a parallel set of literature which has accounted for this additional dispersion by accounting for the structural variations typically expected in a real monolith. For example, Ahn and Brandani (2005) were able to account for the additional dispersion observed in the experimental breakthrough by considering normally distributed channel sizes and adsorbent layer thicknesses. The channel size distribution meant that the individual channels had different interstitial fluid flow velocities and thus different breakthrough curves. The experimental breakthrough curve was the weighted average of these individual breakthroughs. Crittenden et al. (2011) also used a normal distribution of channel sizes to partially explain the experimentally observed breakthrough curves. Valdes-Solis et al., (2004) employed a velocity profile across their monolith's cross-section to explain the broader breakthrough curve that they observed in their experiments. The velocity profile may have been introduced by the distribution of channel sizes, as is the case in Ahn and Brandani (2005) and Crittenden, et al. (2011). It is important to note here that though the approach to consider the non-uniformities in channel size and adsorbent loading are relatively accurate, they do demand an additional computation effort as the distribution has to be discretised and the ideal monolith model has to be solved for each one of these discrete set of channels.

This study aims to resolve the inherent inconsistency in having to choose different MTCs to predict breakthrough and cycle performance while providing a quantitative basis for the observations made by Mohammadi (2017). The monolith reported in Mohammadi (2017) has been used as a case study to show that the same experimentally determined true MTC can be used to predict both the breakthrough and the cyclic performance accurately. Due to lack of access to the actual specimen of the monolith, the structure of the channel has been inferred by approximating the experimental breakthrough as a combination of individual breakthrough curves. A slight variation in the adsorbent loading, channel size and inlet flow distribution have been used to account for the additional dispersion and the elongated tail observed in the breakthrough curve. The approach illustrated in this article is thus devoid of any inherent inconsistencies and can be employed to simulate monolith adsorbent systems suffering from significant channel non-uniformities and inlet flow mal-distributions.

### **Monolith column model**

As part of this work, the capability to simulate monolith columns has been added to our in-house modular adsorption cycle simulator-CySim (Friedrich et al., 2013). Figure 1 depicts the schematic of the monolith column, as modelled in CySim. All the channels in a monolith column are grouped into 'n' different types of channels, with two perfectly mixed finite

volumes at the two ends. The monolith column model involves each type of channel being solved simultaneously with flow splitting and averaging at the inlet and the outlet of the monolith column, respectively. At the inlet, the flow is split by assuming the same pressure drop across all types of channels. From the Darcy-Weisbach equation (Eq. 1), the ratio of velocities in the individual types of channels is estimated as a function of channel dimensions (Ahn and Brandani 2005; Crittenden et al., 2011).

$$\frac{dP}{dz} = 2fRe \frac{v \eta}{D_{ch}^2} \quad (1)$$

Where,

$f$ : Fanning friction factor

$Re$ : Reynolds number

$v$ : Interstitial velocity in the sinusoidal channel (m/s)

$\eta$ : Dynamic viscosity of the gas (Pa s)

$D_{ch}$ : Characteristic dimension or the hydraulic diameter of the sinusoidal channel (m)

Each type of channel is then solved simultaneously, as per the equations detailed in Friedrich et al. (2013) and reproduced in Appendix I. The flow coming out of individual types of channels is averaged to calculate the outlet flow and concentration from the monolith column.

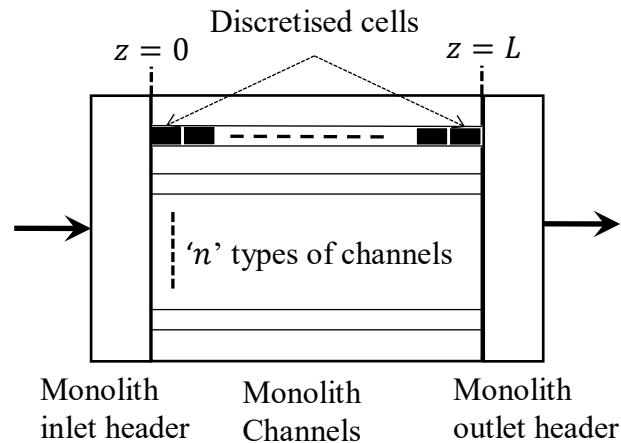


Figure 1: Monolith column schematic, as modelled in CySim

### The Ideal monolith approach:

Figure 2 shows the corrugated monolith structure that has been used as the case study. The monolith was supplied by CATACEL and constructed by wrapping a thin corrugated metal foil layer over a central rod. A layer of zeolite 13X was then coated onto the wrapped metal foil (Mohammadi, 2017). As stated earlier, every channel is considered identical in the ideal monolith approach. In this study, the authors have approximated the representative channel as a sinusoidal channel with an aspect ratio ( $b/a$ ) of  $\sqrt{3}/2$ . Table 1 reproduces the monolith characteristics and the breakthrough experimental conditions.

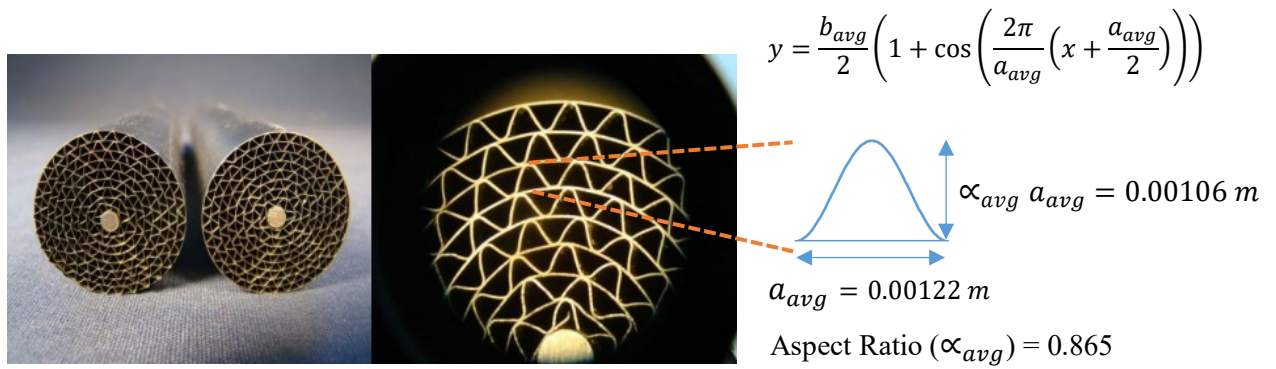


Figure 2: The corrugated monolith structure in the case study (from Mohammadi, 2017), along with the approximated free cross-section of an average sinusoidal channel.

Table 1: Monolith characteristics and breakthrough conditions (Mohammadi, 2017)

Attribute	Value	Remarks
Corrugated monolith characteristics		
Cross-sectional diameter	0.0381 m	
Single core length	0.1524 m	Three of these single cores are used in series, making the total length 0.4572 m
Cell density (channels per square inch)	741	Total number of channels = cell density * monolith cross-sectional area (~1309)
Representative adsorbent layer thickness	0.000051 m	Mohammadi (2017) reduced the adsorbent layer thickness to 0.000031 m to account for partial deactivation due to water adsorption. In this study, the authors have however adjusted the adsorption equilibrium to match the first moment, as observed in the breakthrough curve.
Average bulk porosity of individual channel ( $\epsilon_{bulk,avg}$ )	0.763	The fraction of the adsorbent area in the total (adsorbent and free) cross-sectional area
Average base length of the sinusoidal channel ( $a_{avg}$ )	0.00122 m	Mohammadi (2017) approximated the channels as equilateral triangles, with 0.00122 m as base length. The same has been taken as the base length of the sinusoidal channel.
Average aspect ratio ( $\alpha_{avg}$ )	0.865	The aspect ratio (height/base) of an equilateral triangle
Porosity of the adsorbent layer ( $\epsilon_{ad}$ )	0.54	
Breakthrough experimental conditions		
Feed flow rate	0.00744 mol/s	
Feed Temperature	293.15 K	
Feed Pressure	1.172 bar	
N <sub>2</sub> :CO <sub>2</sub> mole fraction	0.95:0.05	

As per the ideal monolith approach, the monolith has been modelled with the help of a single representative channel under the following set of assumptions:

- Ideal gas behaviour
- Fully developed laminar flow in individual channels
- Isothermal operation- Mohammadi (2017) validated this by experimentally measuring the temperature swing between adsorption and desorption steps of a VPSA cycle.
- 1-D axially dispersed plug flow for the bulk fluid phase
- The pure isotherm data reported in Mohammadi (2017) has been fitted to a dual-site Langmuir model and the parameters thus obtained, have been reported in Table A1 (Appendix II).
- 1-D diffusion in the adsorbent layer with mass transfer rate given by the LDF model - A 1-D diffusion has been assumed in the adsorbent layer, which is consistent with the same assumption made in Mohammadi (2017). This has also been corroborated by Mennitto et al. (2018), where they suggest that the 3-D mass transfer may be approximated by an equivalent 1-D diffusion in the solid layer by redistributing the extra adsorbent in the corners and at the top of the sinusoidal channel to the sides of a similar equilateral triangle. Mohammadi (2017) reported a Linear Driving Force (LDF) MTC of  $1 \text{ s}^{-1}$  for both  $\text{CO}_2$  and  $\text{N}_2$  which they measured from frequency response experiments.
- Gas diffusion in the adsorbent layer controls the overall rate of mass transfer, with the adsorbent being in equilibrium with adsorbent layer fluid
- The pressure gradient in the axial direction is given by the Darcy-Weisbach equation (Eq. 1). For a sinusoidal channel, the characteristic dimension (or hydraulic diameter), and the product of the fanning friction factor and the Reynold's number is given as follows:

$$fRe = -1.2991 \alpha^2 + 5.4238 \alpha + 8.8714; \quad 0.125 \leq \alpha \leq 2 \quad (\text{For a sinusoidal channel: obtained from data points reported in Shah and London, 1971}) \quad (2)$$

$$D_{ch} = a(1.0542 - 0.4660 \alpha - 0.1180 \alpha^2 + 0.1794 \alpha^3 - 0.0436 \alpha^4); \quad (\text{Chung et al., 2009}) \quad (3)$$

Figure 3 shows the predicted  $\text{CO}_2$  breakthrough curve, using an LDF constant of  $1 \text{ s}^{-1}$  for both  $\text{CO}_2$  and  $\text{N}_2$ . As is evident from the breakthrough curve, the breakthrough curve is a lot steeper than what is observed experimentally. However, if the LDF constant is artificially reduced by a hundred times, the experimental breakthrough can be reasonably matched, except for the two initial 'kinks' on the breakthrough curve. However, as Mohammadi (2017) recently found out, using the reduced MTC may grossly under-estimate the cyclic performance. It is the primary aim of this work to demonstrate how both the experimental breakthrough and the cyclic performance can be reasonably predicted with the true MTC, by incorporating the effect of channel non-uniformities and inlet flow mal-distribution in the monolith channel model.

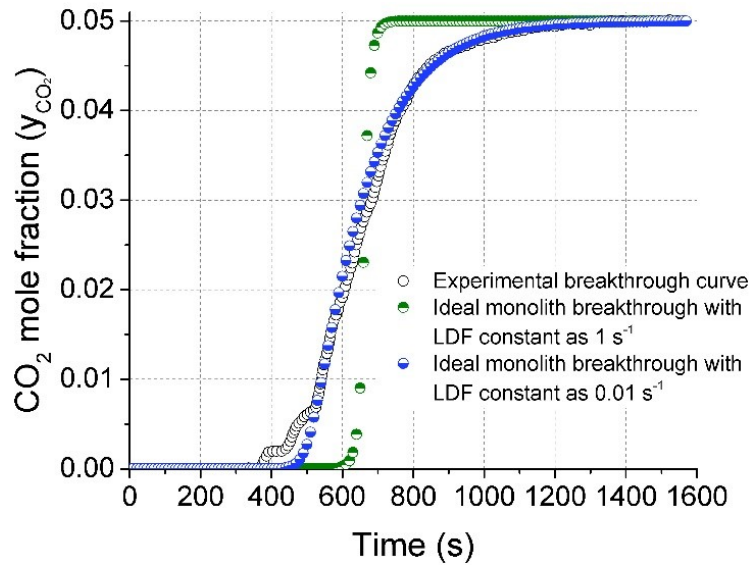


Figure 3: The experimental CO<sub>2</sub> breakthrough curve reported by Mohammadi (2017) and the simulated breakthrough curve corresponding to the true ( $1 \text{ s}^{-1}$ ) and reduced ( $0.01 \text{ s}^{-1}$ ) MTC

### The ‘real’ monolith approach

The real monolith approach has been defined as the approach which takes into account the structural non-uniformities across different channels of the monolith. Due to lack of access to the original monolith and the experimental set-up, the exact grouping of the channels is impossible. However, certain reasonable and logical deductions about the structure of the channels may be drawn through a thorough analysis of the experimentally observed breakthrough curve.

#### *Breakthrough deconvolution*

Figure 4 reproduces the experimental breakthrough reported by Mohammadi (2017) for a closer inspection.

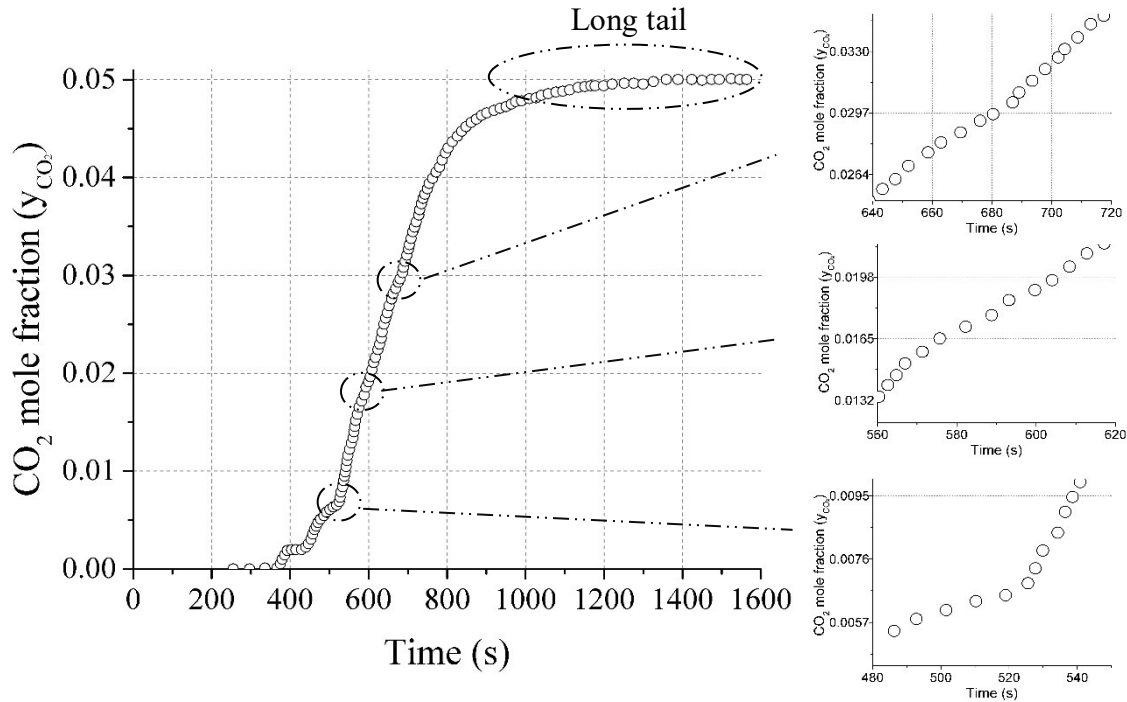


Figure 4: The experimental breakthrough curve, as measured by Mohammadi (2017), for the corrugated monolith shown in Figure 2. Feed: CO<sub>2</sub> and N<sub>2</sub> mixture with mole fractions being 0.05 and 0.95, respectively

The three essential things to note from the breakthrough curves are as follows:

1. *The First kink:* The first kink in the breakthrough curve at  $\sim 400$  s suggests some form of flow bypass. A potential source of this bypass could be the gap between the monolith core (shown in Figure 2) and the encasing cylinder.
2. *The overall breakthrough as a combination of individual breakthrough curves:* After the initial kink, there are at least three instances when the breakthrough curve shifts trajectory. It is likely that there is a continuous distribution in channel sizes and adsorbent loadings. However, to ensure a reasonable computation complexity, only three such instances have been considered in this study. They have been highlighted in Figure 4. Thus the overall breakthrough curve may be deconvoluted into at least four individual breakthrough curves corresponding to four different sets (or 'types') of channels, each corresponding to a particular channel dimension and adsorbent loading. In other words, at least four different groups (or types) of channels may be formed, with each group modelled via a representative channel. An average at the outlet of all the type of channels can then be done to generate the overall breakthrough.
3. *The long tail of the breakthrough curve:* Heat effects could be one of the reasons for the long tail of the breakthrough curve. However, Mohammadi (2017) in their analysis confirmed that the high thermal conductivity of the base metal foil implies that any heat generated during adsorption is quickly absorbed and dissipated throughout the matrix. The other probable reason for the long tail could be inlet flow mal-distribution, caused by a pressure profile across the cross-section of the corrugated monolith. The entire cross-section of the monolith has been hypothesised to consist of just two sectors, viz. an inner and an outer sector (Figure 5), to limit the computation effort.

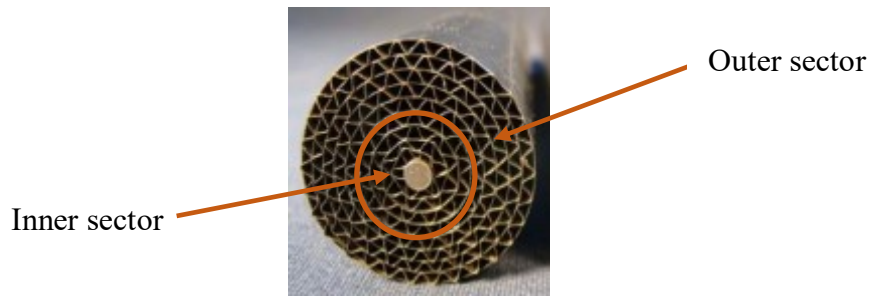


Figure 5: Two representative sections of the monolith cross-section to account for inlet flow mal-distribution. Note: The regions have not been drawn to scale.

Based on the points of trajectory change in the breakthrough curve, the overall breakthrough curve has been disintegrated into four individual breakthrough curves until about 950 s, corresponding to four types of channels. The different types of channels have been termed as Type I, II, III and IV, respectively.

At this stage, two additional assumptions have been made, viz.:

1. Type I channels, having the fastest breakthrough are the innermost set of channels in the inner sector. As mentioned in Mohammadi (2017), the monolith was constructed by wrapping a thin corrugated metal foil layer over a central rod. During such a construction process, the central channels often tend to deform in a way that the aspect ratio ( $\alpha$ ) decreases, while the base dimension ( $a$ ) increases. The earlier breakthrough of Type I channels has been attributed to this change in the structure. The adsorbent loading in Type I channels has been assumed to be the same as the average value reported in Table 1.
2. It has been assumed that apart from the innermost channels of the inner sector (i.e. Type I channels), both the inner and the outer sector are composed of the same types of channels, i.e. Type II, III and IV, and in the same proportion. It has been further assumed that there is a variation of  $\pm 5\%$  in adsorbent loading across Type II, III and IV channels, with Type III representing the average loading, as reported in Table 1. The total (adsorbent + free) cross-sectional area of individual Type I, II, III and IV channels has been assumed to be the same and has been calculated through the average value of ' $\alpha$ ' and ' $a$ ' reported in Table 1.

Table 2 summarises the individual channel's porosity, free and total cross-sectional for channels of different types.

Table 2: Porosity, individual channel's total, and free cross-sectional area

	Type I	Type II	Type III	Type IV
Porosity ( $\epsilon$ )	0.76300 (Average value)	0.77485 (-5% solid loading)	0.76300 (Average value)	0.75115 (+5% solid loading)
Individual channel's total (adsorbent + free) cross-section area $\left( A_{T,i} = \frac{A_{f,i}}{\epsilon_{bulk,i}} \right)$	$8.437 \times 10^{-7} \text{ m}^2$			
Individual channel's free cross-section area $\left( A_{free,i} = \frac{\alpha_i a_i^2}{2} \right)$	$6.437 \times 10^{-7} \text{ m}^2$	$6.537 \times 10^{-7} \text{ m}^2$	$6.437 \times 10^{-7} \text{ m}^2$	$6.337 \times 10^{-7} \text{ m}^2$

A reasonable estimate of individual breakthrough curves has then been obtained from the overall breakthrough curve in step by step manner. The first two steps have been explicitly illustrated for Type I channels.

Step I: Estimating the flow through each type of channel

It is clear that by the time Type I channels start to breakthrough, the bypass channel has completely broken through. Since the feed is very dilute in CO<sub>2</sub>, the bypass flow rate can then be estimated by taking the weighted average of the outlet concentrations at a time just higher than the time at which the bypass flow completely breaks through. For example, at any time between 400 and 430 s, Eq. (4) can be applied to yield the approximate bypass flow.

$$F_{bypass} y_{bypass,CO_2} + (F_f - F_{bypass}) y_{f-bypass} = F_f y_{bypass,CO_2}^{sat} \quad (4)$$

Where,

$F_{bypass}$ : Approximate bypass flow rate (mol/s)

$y_{bypass,CO_2}$  (= 0.05): CO<sub>2</sub> mole fraction in the bypass outlet stream. This is equal to the feed mole fraction, i.e. 0.05

$F_f$  (= 0.00744): Feed flow rate (mol/s)

$y_{(f-bypass)}$  (= 0): Average CO<sub>2</sub> mole fraction in the outlet flow, apart from the bypass flow. Since none of the other channels breaks through at this point, its value is 0

$y_{bypass,CO_2}^{sat}$  (= 0.002): The saturation mole fraction of CO<sub>2</sub>, if only the bypass breaks through completely. This value is read from the overall breakthrough curve

Therefore,  $F_{bypass} = 0.00030 \text{ mol/s}$

The situation is a bit more complicated for Type I channels as there is no clear demarcation between breakthrough curves of Type I and Type II channels. For this purpose, the overall

breakthrough curve between 430 and 520 s has been extrapolated beyond 520 s, assuming that just the bypass and Type I channels breakthrough, as depicted in Figure 6. This extrapolation yields an estimate of the flow passing through Type I channels by repeating the exercise that was earlier performed for bypass flow estimation.

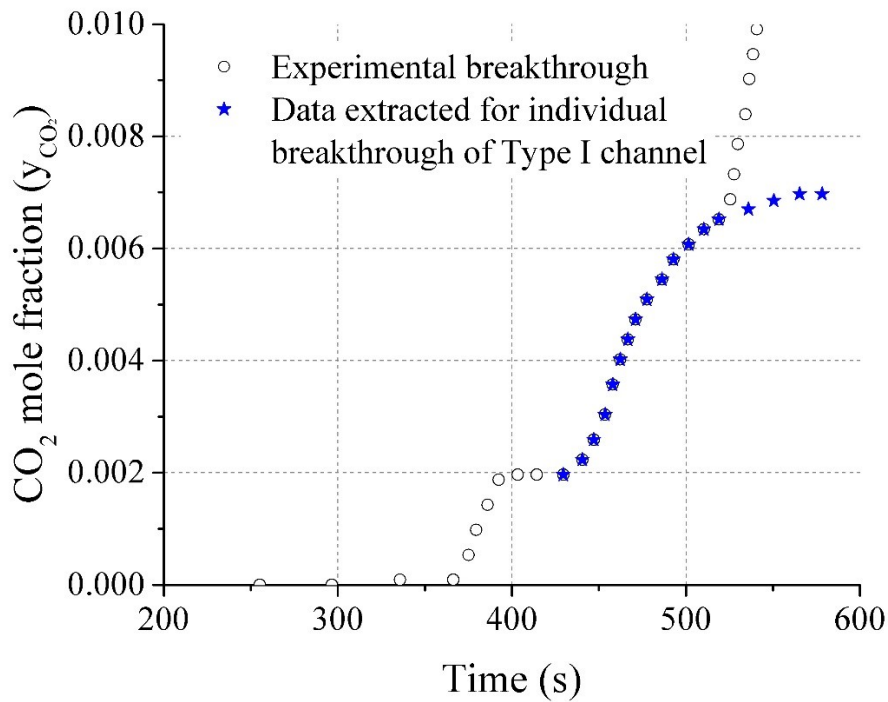


Figure 6: Breakthrough extrapolation for Type I channel

Therefore,  $F_I = 0.00074 \text{ mol/s}$

The same strategy has been applied to calculate the flow rates through Type II, III and IV. Therefore,  $F_{II} = 0.00231 \text{ mol/s}$ ,  $F_{III} = 0.00171 \text{ mol/s}$  and  $F_{IV} = 0.0020 \text{ mol/s}$ .

Step II: Estimating the breakthrough curve for individual types of channels

The points extracted in the first step have been deconvoluted to single out the contribution from an individual type of channel. This step has been illustrated for Type I channels in Table 3.

Table 3: Data deconvolution to obtain individual breakthrough of Type I channels

Time (s)	CO <sub>2</sub> mole fraction at monolith outlet (experimental breakthrough), $y_{T,CO_2}^{exp}$	CO <sub>2</sub> mole fraction in bypass outlet stream, $y_{bypass,CO_2}$	CO <sub>2</sub> mole fraction in Type I outlet stream, $y_{I,CO_2}$
429.60	0.00196	0.0500	$0$ $\left( \frac{F_f y_{tot,CO_2}^{exp} - F_{bypass} y_{bypass,CO_2}}{F_I} \right)$
440.50	0.00223	0.0500	0.00231
447.00	0.00259	0.0500	0.00593
453.60	0.00304	0.0500	0.01045
458.00	0.00357	0.0500	0.01578
462.30	0.00402	0.0500	0.02031
466.60	0.00438	0.0500	0.02393
471.00	0.00473	0.0500	0.02744
477.50	0.00509	0.0500	0.03107
486.30	0.00545	0.0500	0.03469
492.80	0.00580	0.0500	0.03820
501.50	0.00607	0.0500	0.04092
510.30	0.00634	0.0500	0.04363
519.00	0.00652	0.0500	0.04544
535.90	0.00670	0.0500	0.04725
550.50	0.00689	0.0500	0.04836
565.40	0.00697	0.0500	0.05000
578.20	0.00697	0.0500	0.05000

The first moment of the individual breakthrough curves has then been estimated from data points thus obtained, as per the integral in Eq. (5).

$$\mu_i = \int_0^\infty \left( 1 - \frac{y_{i,CO_2}}{y_{f,CO_2}} \right) dt = \frac{L}{v_i} \left[ 1 + \frac{(1-\varepsilon_{bulk,i})}{\varepsilon_{bulk,i}} \left( \frac{q_{f,CO_2}^*}{c_{f,CO_2}} \right) \right] \quad (5)$$

Where,

$\mu_i$ : First moment of the breakthrough curve for Type  $i$  channels (s)

$y_{i,CO_2}$ : CO<sub>2</sub> mole fraction in Type  $i$  outlet stream

$y_{f,CO_2}$ : CO<sub>2</sub> mole fraction in feed stream

$L$ : Length of the monolith column (m)

$\varepsilon_i$ : Bulk porosity for Type  $i$  channels

$q_{f,CO_2}^*$ : Adsorbed amount in equilibrium (with feed concentration) (mol/m<sup>3</sup>)

$c_{f,CO_2}$ : Feed concentration (mol/m<sup>3</sup>)

Therefore,  $\mu_I = 476.00$  s,  $\mu_{II} = 577.01$  s,  $\mu_{III} = 667.1563$  s and  $\mu_{IV} = 774.6352$  s.

Step III: Decoding the channel structure and flow distribution

Using the porosity and the first moment values, Eq. (5) has been used to estimate the velocity ratio in different types of channels.

Therefore,

$$\frac{v_I}{v_{III}} = 1.40, \frac{v_{II}}{v_{III}} = 1.08 \text{ and } \frac{v_{IV}}{v_{III}} = 0.92$$

The velocity ratio is also related to the flow rate, individual channel and free cross-sectional area:

$$\begin{aligned} \frac{v_I}{v_{III}} &= \frac{F_I}{N_I A_{free,I}} \frac{N_{III} A_{free,III}}{F_{III}} \\ \frac{v_{II}}{v_{III}} &= \frac{F_{II}}{N_{II} A_{free,II}} \frac{N_{III} A_{free,III}}{F_{III}} \\ \frac{v_{IV}}{v_{III}} &= \frac{F_{IV}}{N_{IV} A_{free,IV}} \frac{N_{III} A_{free,III}}{F_{III}} \end{aligned} \quad (6)$$

Where,

$N_I, N_{II}, N_{III}$  and  $N_{IV}$  are the number of channels of Type I, II, III and IV, respectively

The previously obtained ratios, when used in Eq. (6), yields the following ratios for the number of channels of different types.

$$\frac{N_I}{N_{III}} = 0.309, \frac{N_{II}}{N_{III}} = 1.232 \text{ and } \frac{N_{IV}}{N_{III}} = 1.288$$

This gives the relative fraction of Type I, II, III and IV channels as follows:

In the inner sector-

$$\frac{N_I}{\sum N_i} = 0.0807, \frac{N_{II}}{\sum N_i} = 0.3218, \frac{N_{III}}{\sum N_i} = 0.2612 \text{ and } \frac{N_{IV}}{\sum N_i} = 0.3364$$

In the outer sector-

$$\frac{N_{II}}{\sum N_i} = 0.3500, \frac{N_{III}}{\sum N_i} = 0.2841 \text{ and } \frac{N_{IV}}{\sum N_i} = 0.3659$$

The velocity ratio is also related to channel geometry via the Darcy-Weisbach equation (Eq. 1). All the channels, within a particular sector, can be assumed to have the same pressure drop across their entire length. This gives Eq. (7) as follows:

$$\begin{aligned} \frac{v_I}{v_{III}} &= \frac{D_{ch,1}^2 f Re_3}{f Re_1 D_{ch,3}^2} \\ \frac{v_{II}}{v_{III}} &= \frac{D_{ch,2}^2 f Re_3}{f Re_2 D_{ch,3}^2} \\ \frac{v_{IV}}{v_{III}} &= \frac{D_{ch,4}^2 f Re_3}{f Re_4 D_{ch,3}^2} \end{aligned} \quad (7)$$

Eq. (7), when solved along with Eqs. (2) and (3), yields the following base dimension and aspect ratio for different types of channels:

$$\alpha_I = 0.7400 \text{ and } a_I = 0.001319 \text{ m}$$

$$\alpha_{II} = 0.8412 \text{ and } a_{II} = 0.001247 \text{ m}$$

$$\alpha_{III} = 0.8650 \text{ and } a_{III} = 0.001220 \text{ m}$$

$$\alpha_{IV} = 0.8916 \text{ and } a_{IV} = 0.001192 \text{ m}$$

Figure 7 shows the free cross-section of the four types of channels, drawn to the same scale. To a naked eye, these channels might appear to be indistinguishable, except for the Type I channel, which appears a bit squished. This is corroborated by the fact that the channels in the actual monolith (Figures 2 and 5) also appear quite similar. As would be explained in the next section, even these minor variations, along with inlet flow mal-distribution, can account for the broad nature of the breakthrough curve.



Figure 7: Free cross-section of an individual channel of Type I, II, III and IV

## Results and Discussion

At this stage, the flow and channel split, amongst the inner and the outer sector of the monolith are the only two degrees of freedom. The two splits have thus been adjusted as parameters to reasonably match the experimentally observed breakthrough curve as shown in Figure 8. The predicted breakthrough in Figure 8 corresponds to flow and channel split of 2.66:1 and 1.88:1, respectively, between the inner and the outer sector of the monolith.

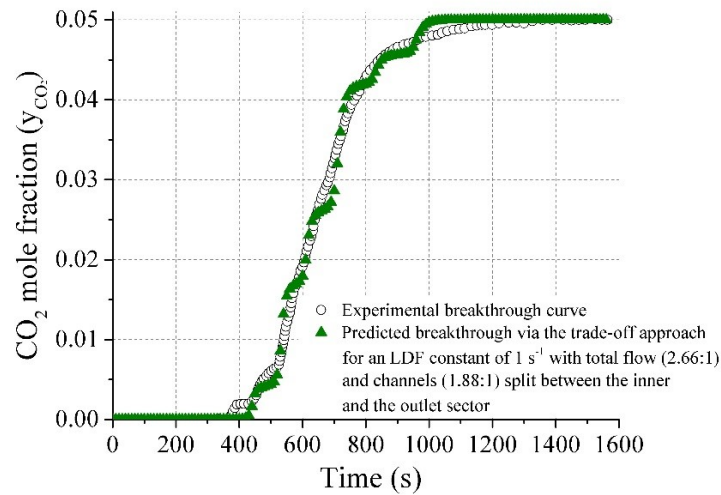
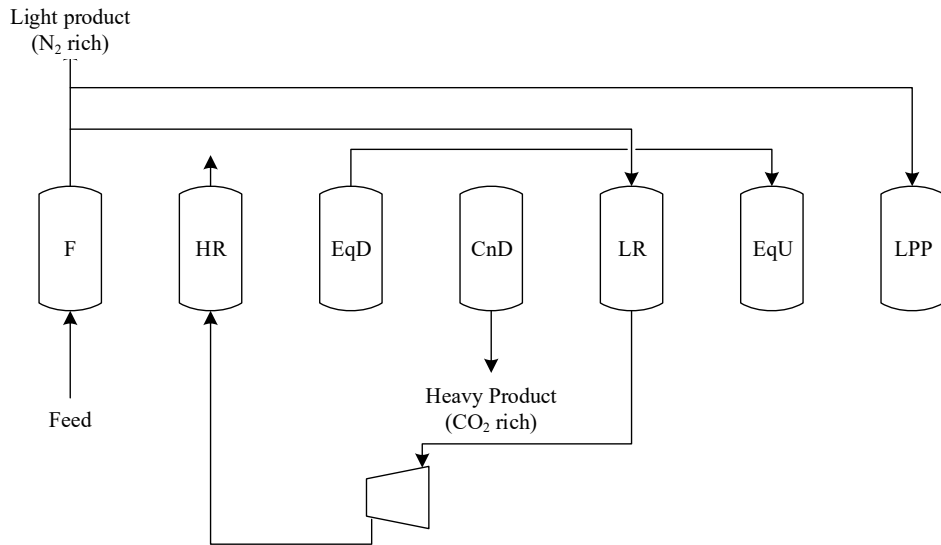


Figure 8: Experimental and predicted breakthrough with the true MTC; flow and channel split of 2.66:1 and 1.88:1, respectively, between the inner and the outer sector

The demarcation between the individual breakthrough curves is visible on the predicted breakthrough curve. A continuous distribution of channel size, adsorbent loading and inlet flow would have resulted in much smoother transitions between the individual breakthrough curves, while also requiring a significantly greater computation effort. The bypass flow has not been modelled as its relative contribution towards the breakthrough curve was negligible. The non-agreement towards the end of the breakthrough tail refers to the fact that the two sectors might not be enough to explain the extended tail fully. However, since the relative flow through these additional sectors also appears to be small, incorporating them into the model would not be computationally efficient. The predicted breakthrough represents a significant improvement over the breakthrough predicted via the ideal monolith approach using the true MTC of  $1 \text{ s}^{-1}$ .

As stated earlier, this work aims to remove the inherent inconsistency in choosing different MTCs to predict breakthrough and cyclic performance. After achieving a reasonable agreement between the experimental and the simulated breakthrough curve, full-cycle simulations have thus been performed using the true MTC of  $1 \text{ s}^{-1}$ . Figure 9 reports the 3-bed, 6-step cycle and its schedule, as reported by Mohammadi (2017). Table 4 reports the experimental conditions for the different runs performed by Mohammadi (2017). Table 5 reports the cyclic experimental performance, along with the predictions made via the ideal (Mohammadi, 2017) and the real monolith approach (this study).



Feed			HR	EqD	CnD	LR	EqU	LPP
HR	EqD	CnD	LR	EqU	LPP	Feed		
LR	EqU	LPP	Feed			HR	EqD	CnD

Figure 9: The 3-bed, 6-step VPSA cycle reported by Mohammadi (2017). HR: heavy reflux, EqD: pressure equalisation depressurisation, CnD: counter-current depressurisation, LR: light reflux, EqU: pressure equalisation pressurisation and LPP: light product pressurisation. Feed pressure = 1.179 bar, CO<sub>2</sub> production pressure = 0.04 bar and N<sub>2</sub>:CO<sub>2</sub> mole fraction in the feed = 0.8408:0.1592

Table 4: VPSA experiments performed by Mohammadi (2017).

Run no.	Step Times (s)				Temperature (K)	Throughput (L <sub>STP</sub> /h/kg)
	Feed	HR and LR	EqD and EqU	CnD and LPP		
1	40.00	20.00	6.67	13.33	338.15	4060.19
2	48.00	24.00	8.00	16.00	338.15	3383.49
3	48.00	20.00	8.00	20.00	338.15	3383.49
4	48.00	20.00	8.00	20.00	338.15	4060.19
5	80.00	40.00	13.33	26.67	338.15	2030.10
6	80.00	40.00	13.33	26.67	338.15	2436.11
7	80.00	40.00	13.33	26.67	294.15	2436.11

Table 5: Experimental CO<sub>2</sub> purities and recoveries against those predicted using the ideal (Mohammadi, 2017) and the real monolith approach (this study). ECP: experimental CO<sub>2</sub> purity, SCP: simulated CO<sub>2</sub> purity, ECR: experimental CO<sub>2</sub> recovery and SCR: simulated CO<sub>2</sub> recovery. The true MTC of 1 s<sup>-1</sup> has been used in both the approaches.

Run no.	ECP (%)	SCP via the ideal monolith approach (Mohammadi, 2017) (%)	SCP via the real monolith approach (this study) (%)	ECR (%)	SCR via the ideal monolith approach (Mohammadi, 2017) (%)	SCR via the real monolith approach (this study) (%)
1	88.26	87.84	87.66	94.90	95.74	93.86
2	86.30	87.83	87.7	93.59	95.87	94.12
3	86.05	87.64	87.59	94.01	94.75	93.51
4	89.00	90.48	89.35	87.07	93.65	89.21
5	87.79	87.87	88.70	96.36	96.17	94.38
6	91.31	90.77	90.66	94.00	95.55	92.39
7	88.56	88.83	86.67	94.70	94.75	94.41

Figure 10 (a) and (b) show the extent to which the predicted cyclic performances, via the two approaches, deviated from the experimental observations. Both the approaches have been able to predict CO<sub>2</sub> purities within a limit of  $\pm 2.5\%$  deviation. However, a relatively larger deviation has been observed in the predicted CO<sub>2</sub> recoveries, especially for the experimental run no. 4. Following the ideal monolith approach, Mohammadi (2017) predicted a CO<sub>2</sub> recovery which was  $\sim 7.5\%$  higher than what was experimentally observed. They explained it qualitatively through the additional dispersion caused by non-uniformities in channel size, shape and adsorbent loading. They hypothesised that due to the high throughput in run no. 4, the adsorption front might have been pushed substantially towards the light product end. The high penetration of the adsorption front meant that a significant portion of the heavy product (CO<sub>2</sub>) was lost along with the light product due to the additional dispersion caused by channel non-uniformities, leading to a lower than expected CO<sub>2</sub> recovery. The real monolith approach attempts to quantify this loss and predict a CO<sub>2</sub> recovery which is much closer to the experimental observation while using the same MTC, as was used for breakthrough prediction. The CO<sub>2</sub> recoveries predicted via the real monolith approach deviate from the experimental observations within a limit of  $\pm 2.5\%$ .

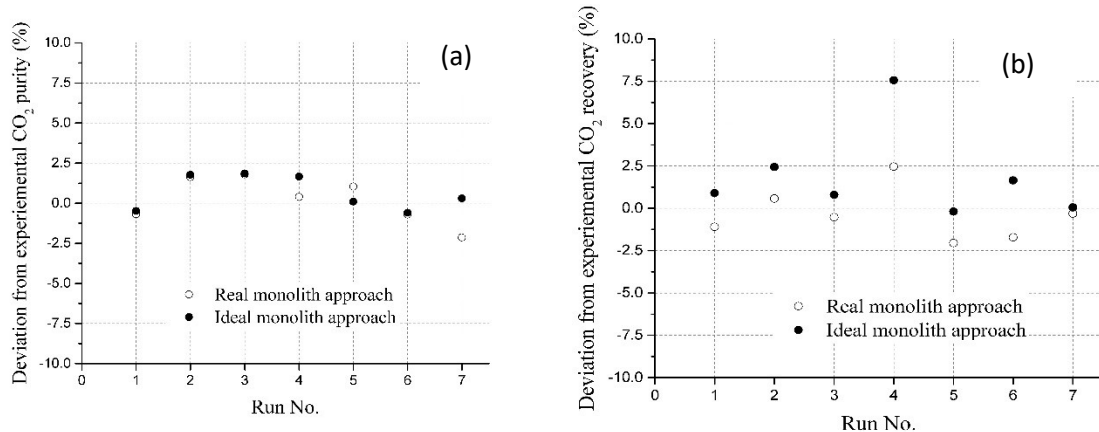


Figure 10: Extent of deviation of predicted (a) CO<sub>2</sub> purities and (b) CO<sub>2</sub> recoveries from experimental observations

The real monolith approach is thus able to provide a quantitative basis for the explanation reported by Mohammadi (2017). In real life applications, monolith columns are expected to be operated at a high throughput, as their primary application is after all in the intensification of adsorption-based processes. This makes it imperative to incorporate the effect of significant monolith non-uniformities in the mathematical models to ensure that they are a true representation of the underlying physical phenomenon. It further ensures that both the breakthrough and full-cycle performance can be reasonably predicted while using the same (and true) MTC. However, this also increases the computation effort, as now effectively the single monolith column is modelled as multiple monolith columns operating in parallel. It is for this reason that the ideal monolith approach might still be preferred if the non-uniformities are not significant enough. However, as noted earlier, getting rid of such non-uniformities might be impossible as they are invariably introduced during monolith preparation. In such a case, a judicious assessment of the breakthrough might yield useful insights on how to efficiently model the system, while keeping the number of columns low.

## Conclusions

Structure adsorbents, like monoliths, are essential to achieving intensification of adsorption-based processes. The uniformity in channel size and adsorbent loading is often assumed while modelling monolithic adsorbent columns. It implies that all the channels of the monolith behave identically and the entire system can be modelled by extrapolating the performance of a single channel. This has been referred to as the ideal monolith approach in this article. However, this assumption may often be invalid as non-uniformities are invariably introduced into the monolith during its manufacturing. In addition to channel non-uniformities, any inlet flow mal-distribution can also affect the monolith's performance by substantially increasing the dispersion of the concentration front. Traditionally, this additional dispersion is accounted for by assuming an effective MTC which can be substantially lower than its true value. However, as noted by a recent study (Mohammadi, 2017), this effective MTC cannot predict the cyclic performance. The cyclic performance can be reasonably predicted only by using the true MTC. This presents an inherent inconsistency in the ideal monolith approach, wherein different MTC are needed to predict the same underlying physical phenomenon. Even while

using the true MTC, the full-cycle predictions made via the ideal monolith approach have been observed to substantially deviate from the experimental observations, especially for high throughput operation. This highlights the importance of incorporating the effect of such non-uniformities and flow mal-distribution while modelling monolith columns, as their primary application is in high throughput applications.

This article illustrates the real monolith approach, which in part accounts for the channel non-uniformities and flow mal-distribution. The corrugated monolith reported by Mohammadi (2017) has been used as a case study to illustrate the approach. The experimentally observed breakthrough curve has been deconvoluted into individual breakthrough curves, corresponding to different groups (or types) of channels. The ratio of interstitial velocity in different types of channels has then been estimated using the fluid mean residence time (predicted from the individual breakthrough points) while assuming a  $\pm 5$  % variation in adsorbent loading across the different types of channels. The velocity ratio has also been used to estimate the fractional coverage of different types of channels and their respective sizes. In the absence of heat-effects, the long tail observed in the breakthrough curve has been attributed to inlet flow mal-distribution. The monolith has been assumed to consist of two sectors, viz. an inner and an outer one. The channel and flow split between the inner and outer sector have been adjusted to get a reasonable agreement between the predicted and experimentally observed breakthrough curve, without the need to adjust the true MTC.

The monolith structure thus estimated has been used to predict the performance of a VPSA cycle for  $N_2$  and  $CO_2$  separation. Except for a high throughput case, Mohammadi (2017) had reported a reasonable agreement between the results predicted through the ideal monolith approach (with the true MTC), and experimental observations. At high throughput operation, the additional dispersion caused by channel non-uniformities and flow mal-distributions can result in significant loss of the heavy product ( $CO_2$ ) along with the light product ( $N_2$ ). Since the ideal monolith approach, with the true MTC, does not account for this additional dispersion, it predicts a higher than observed heavy product recovery. By accounting for this additional dispersion, the real monolith approach has been shown to predict the cyclic performances within a limit of  $\pm 2.5$  % from the experimental observations. In summary, this article illustrates the real monolith approach to model the monolith columns, by incorporating the effect of channel non-uniformities and flow mal-distributions. Since this approach better approximates the underlying physical phenomenon, it can be used to predict both the breakthrough and cyclic performance of a monolith with the help of a single MTC.

## **Acknowledgements**

The authors would like to acknowledge the financial support from Engineering and Physical Sciences Research Council, under grant no. EP/N024613/1.

## References

- Ahn, H., and Brandani, S. (2005). Dynamics of Carbon Dioxide Breakthrough in a Carbon Monolith. *Adsorption*, *11*, 473-477. doi: 10.1007/s10450-005-5970-z
- Chung, J. D., Lee, D.-Y., and Yoon, S. M. (2009). Optimization of desiccant wheel speed and area ratio of regeneration to dehumidification as a function of regeneration temperature. *Solar Energy*, *83*, 625-635. doi:10.1016/j.solener.2008.10.011
- Crittenden, B., Camus, O., Perera, S., Mays, T., Sa'nchez-Liarte, F., Tennison, S., and Crezee, E. (2011). Nonuniform Channels in Adsorbent Monoliths. *AIChE*, *57*(5), 1163-1172. doi: 10.1002/aic.12335
- Xebec. (2018). *Rapid Cycle Pressure Swing Adsorption (RCPSA)*. Retrieved from Xebec Adsorption Inc.: [https://www.xebecinc.com/fr/pdf/e\\_h2x\\_6200\\_brochure.pdf](https://www.xebecinc.com/fr/pdf/e_h2x_6200_brochure.pdf) (accessed: 12/12/2018)
- Friedrich, D., Ferrari, M.-C., and Brandani, S. (2013). Efficient Simulation and Acceleration of Convergence for a Dual Piston Pressure Swing Adsorption System. *Ind. Eng. Chem. Res*, *52*, 8897-8905. doi:10.1021/ie3036349
- Gulijk, C. v., Linnders, M., Vald'es-Sol'is, T., and Kapteijn, F. (2005). Intrinsic channel maldistribution in monolithic. *Chemical Engineering Journal*, *109*, 89-96. doi: 10.1016/j.cej.2005.03.013
- InvenTys Inc. (2017). *Discover VeloxoTherm™*. Retrieved from: <http://inventysinc.com/veloxotherm/> (accessed: August 22, 2017)
- Lopes, J. P., and Rodrigues, A. (2016). Monolith Reactors. In Z. I. Önsan, and A. K. Avci, *Multiphase Catalytic Reactors: Theory, Design, Manufacturing, and Applications* (pp. 173-212). New Jersey: John Wiley & Sons, Inc.
- Mohammadi, N. (2017). CO<sub>2</sub> capture from flue gas by a PSA process using a novel structured adsorbent. *Doctoral Thesis*.
- Naturally Resourceful. (2017). *Inventys: Saving the world by braving hi-tech's "Valley of Death"*. Retrieved from <http://www.resourceworks.com/inventys> (accessed 22/07/2017)
- Regufe, M. J., Ferreira, A. F., Loureiro, J. M., Shi, Y., Rodrigues, A., and Ribeiro, A. M. (2018). New hybrid composite honeycomb monolith with 13X zeolite and activated carbon for CO<sub>2</sub>. *Adsorption*, *24*, 249-265. doi: 10.1007/s10450-018-9938-1
- Rezaei, F., Mosca, A., Webley, P., Hedlund, J., and Xiao, P. (2010). Comparison of Traditional and Structured Adsorbents for CO<sub>2</sub> Separation by Vacuum-Swing Adsorption. *Ind. Eng. Chem. Res.*, *49*, 4832-4841. doi: 10.1021/ie9016545
- Rezaie, F., and Webley, P. (2010). Structured adsorbents in gas separation processes. *Separation and Purification Technology*, *70*, 243-256. doi: 10.1016/j.seppur.2009.10.004

- Ruthven, D., and Thaeron, C. (1997). Performance of a parallel passage adsorbent contactor. *Separation and Purification Technology*, 12, 43-60. doi: 10.1016/S1383-5866(97)00016-6
- Shah, R., and London, A. (1971). *Laminar flow forces convection heat transfer and flow friction in straight and curved ducts- A summary of analytical solutions*. Stanford University, Department of Mechanical Engineering. Stanford: Stanford University.
- Toreja, J., Chan, N., VanNostrand, B., and Dickinson, J. (2010). *Environmental Experts*. Retrieved from Environmental Experts: <https://www.environmental-expert.com/articles/rotary-valve-fast-cycle-pressure-swing-adsorption-paper-450670> (accessed 12/12/2018)
- Valdes-Solis, T., Linders, M., Kapteijn, F., Marban, G., and Fuertes, A. (2004). Adsorption and breakthrough performance of carbon-coated ceramic monoliths at low concentration of n-butane. *Chemical Engineering Science*, 59, 2791-2800. doi: 10.1016/j.ces.2004.03.025

## Appendix I

### Model equations for a single type of channel

Component mass balance:

$$\frac{\partial c_j}{\partial t} + \frac{(1-\varepsilon_{bulk,i})}{\varepsilon_{bulk,i}} \frac{\partial \bar{Q}_j}{\partial t} + \frac{\partial(v_i c_j)}{\partial z} + \frac{\partial J_j}{\partial z} = 0; \quad (A1)$$

$$\frac{\partial \bar{Q}_j}{\partial t} = k_{LDF,j} (c_j - c_{ad,j}) \quad (A2)$$

$$\varepsilon_{ad} \frac{\partial c_{ad,j}}{\partial t} + (1 - \varepsilon_{ad}) \frac{\partial \bar{Q}_j}{\partial t} = \frac{\partial \bar{Q}_j}{\partial t} \quad (A3)$$

$$\bar{Q}_j = q_j^* (c_{ad,j}) \quad (A4)$$

$$\frac{\partial J_j}{\partial z} = -D_{m,j} c_T \frac{\partial y_j}{\partial z} \quad (A5)$$

Boundary conditions:

$$J_j \Big|_{z=0} = \frac{v_i + |v_i|}{2} \Big|_{z=0} (y_{j,0-} - y_j(0)) c_T$$

$$J_j \Big|_{z=L} = \frac{v_i + |v_i|}{2} \Big|_{z=L} (y_{j,L+} - y_j(L)) c_T \quad (A6)$$

Dual-site Langmuir isotherm:

$$q_j^* = \frac{q_{j,s}^1 b_j^1 p_j}{1 + \sum_{k=1}^{NC} b_k^1 p_k} + \frac{q_{j,s}^2 b_i^2 p_i}{1 + \sum_{k=1}^{NC} b_k^2 p_k} \quad ; \quad b_j^l = b_{j,0}^l \exp\left(\frac{\Delta \tilde{H}_j^l}{RT}\right) \quad (A5)$$

Where,

$b_{j,0}^l$ : Langmuir equilibrium constant for component  $j$  on site  $l$  (1/bar)

$c_{ad,j}$ : Concentration of component  $j$  in the adsorbent layer voids (mol/m<sup>3</sup>)

$c_j$ : Concentration of component  $j$  in bulk fluid phase (mol/m<sup>3</sup>)

$c_T$ : Total concentration in the bulk fluid phase (mol/m<sup>3</sup>)

$D_{m,j}$ : Molecular diffusivity of component  $j$  (m<sup>2</sup>/s)

$J_j$ : Diffusive flux of component  $j$  (mol/m<sup>2</sup>/s)

$k_{LDF,j}$ : LDF mass transfer coefficient for component  $j$  (1/s)

$NC$ : Number of components

$p_j$ : Partial pressure of component  $j$  (bar)

$q_j^*$ : Adsorbed phase concentration of component  $j$  at equilibrium (mol/m<sup>3</sup>)

$q_j$ : Adsorbed phase concentration of component  $j$  (mol/m<sup>3</sup>)

$q_{j,s}^l$ : Saturation capacity of component  $j$  for site  $l$  (mol/m<sup>3</sup>)

$\bar{Q}_j$ : Average concentration of component  $j$  in the adsorbent layer (mol/m<sup>3</sup>)

$\bar{q}_j$ : Average adsorbed phase concentration of component  $j$  (mol/m<sup>3</sup>)

$R$ : Universal gas constant (J/mol/K)

$T$ : Temperature (K)

$t$ : Time (s)

$v_i$ : Interstitial velocity in Type  $i$  channels (m/s)

$y_j$ : Mole fraction of component  $j$  in bulk fluid phase

$z$ : Axial length (m)

$\varepsilon_{bulk,i}$ : Bulk porosity for channels of Type  $i$

$\varepsilon_{ad}$ : Porosity of the adsorbent layer

$\Delta\tilde{H}_j^l$ : Heat of adsorption of component  $j$  on site  $l$  (J/mol)

## Appendix II

Table A1: Dual-site Langmuir isotherm parameters

Parameter	Value
$q_{N_2,s}^1$ (mol/m <sup>3</sup> )	2956.5
$q_{CO_2,s}^1$ (mol/m <sup>3</sup> )	2956.5
$b_{N_2,0}^1$ (1/bar)	0
$b_{CO_2,0}^1$ (1/bar)	0.000001896
$\Delta\tilde{H}_{N_2}^1$ (J/mol)	11171.79
$\Delta\tilde{H}_{CO_2}^1$ (J/mol)	46413.48
$q_{N_2,s}^2$ (mol/m <sup>3</sup> )	5784.132
$q_{CO_2,s}^2$ (mol/m <sup>3</sup> )	5784.132
$b_{N_2,0}^2$ (1/bar)	0.0000332
$b_{CO_2,0}^2$ (1/bar)	0.000001424164
$\Delta\tilde{H}_{N_2}^2$ (J/mol)	18825.74
$\Delta\tilde{H}_{CO_2}^2$ (J/mol)	37654.61